Microstructure refinement - homogenization and flexural strength improvement of Al2O3 ceramics fabricated by DLP-stereolithography integrated with chemical precipitation coating process

Guanglin Nie (nieguanglin@gdut.edu.cn)
Guangdong University of Technology https://orcid.org/0000-0003-2887-2778
Yehua Li
Guangdong University of Technology
Pengfei Sheng
Guangdong University of Technology
Fei Zuo
Guangdong University of Technology
Haolin Wu
Guangdong University of Technology
Leiren Liu
Guangdong University of Technology
Xin Deng
Guangdong University of Technology
Yiwang Bao
China Building Materials Academy
Shanghua Wu
Guangdong University of Technology

Research Article

Keywords: Al2O3 ceramic, stereolithography, flexural strength, reliability, thermal conductivity, microstructure

Posted Date: October 8th, 2020

DOI: https://doi.org/10.21203/rs.3.rs-86507/v1

Version of Record: A version of this preprint was published at Journal of Advanced Ceramics on July 13th, 2021. See the published version at https://doi.org/10.1007/s40145-021-0473-2.

Microstructure refinement - homogenization and flexural strength improvement of Al_2O_3 ceramics fabricated by DLP-stereolithography integrated with chemical precipitation coating process

Guanglin NIE[a, *], Yehua LI[a], Pengfei SHENG[a], Fei ZUO[a], Haolin WU[a], Leiren LIU[a], Xin DENG[a], Yiwang BAO[b], Shanghua WU[a, *]

[a] *School of Electromechanical Engineering, Guangdong University of Technology, Guangzhou 510006, Guangdong, PR China*

[b] *State Key Laboratory of Green Building Materials, China Building Materials Academy, Beijing 100024, PR China*

Abstract: In this study, the chemical precipitation coating (CP) process was creatively integrated with DLP-stereolithography based 3D printing for refining and homogenizing the microstructure of 3D printed Al_2O_3 ceramic. Based on this novel approach, Al_2O_3 powder was coated with a homogeneous layer of amorphous Y_2O_3; with the coated Al_2O_3 powder found to make the microstructure of 3D printed Al_2O_3 ceramic more uniform and refined, as compared with the conventional mechanical mixing (MM) of Al_2O_3 and Y_2O_3 powders. The grain size of Al_2O_3 in Sample CP is 64.44% and 51.43% lower than those in the monolithic Al_2O_3 ceramic (AL) and Sample MM, respectively. Sample CP has the highest flexural strength of 455.37±32.17 MPa, which is 14.85% and 25.45% higher than those of Samples MM and AL, respectively; also Sample CP has the highest Weibull modulus of 16.88 among the three kinds of samples. Moreover, the fine grained Sample CP has a close thermal conductivity to the coarse grained Sample MM because of the changes in morphology of $Y_3Al_5O_{12}$ phase from semi-connected (Sample MM) to isolated (Sample CP). Finally, specially designed fin-type Al_2O_3 ceramic heat sinks were successfully fabricated via the novel integrated process, which

Abbreviations: DLP, digital light processing; MM, mechanical mixing; CP, chemical precipitation coating; AL, Al_2O_3.

* Corresponding author.
E-mail address: nieguanglin@gdut.edu.cn (G. Nie), swu@gdut.edu.cn (S. Wu)

has been proven to be an effective method for fabricating complex-shaped Al_2O_3 ceramic components with enhanced flexural strength and reliability.

Keywords: Al_2O_3 ceramic; stereolithography; flexural strength; reliability; thermal conductivity; microstructure

1 Introduction

Alumina (Al_2O_3) ceramic has been widely used in thermal management applications, such as substrates, heat sinks and packaging materials for integrated circuits and LEDs, due to its high mechanical strength, excellent electrical insulation, high thermal conductivity as well as acceptable cost [1-3]. The power density in modern electronic systems is now increasing at an unprecedented speed, thus it is urgent to fabricate the fin-type Al_2O_3 ceramic heat sinks and microchannel substrates with complex shapes, in order to dissipate heat quickly and protect valuable electronic components effectively. However, the high hardness and low toughness of structural ceramics make it difficult to shape and machine complex-shaped ceramic parts [4]. The conventional ceramic-shaping methods, such as dry pressing, isostatic pressing, gel casting, injection molding etc. [5-7], require the use of molds, leading to increased manufacturing cost [8]; and cannot be used to fabricate Al_2O_3 ceramic parts with highly complex geometries and interconnected channels [9], thereby limiting the wide application of Al_2O_3 components. So there has been strong demand to develop a more effective approach to sidestep the aforementioned limitations and fabricate complex-shaped Al_2O_3 ceramic parts.

Additive manufacturing, also referred to as 3D printing and rapid prototyping, is a series of advanced manufacturing technologies to construct complicated prototypes from 3D CAD models [10]. The introduction of 3D printing technologies into the fabrication of advanced ceramics can address the issues such as mold dependence and difficulties in shaping complex-shaped ceramic parts [8]. Due to the excellent technical advantages of stereolithography such as high dimensional accuracy and good surface finish, efforts on applying stereolithography to ceramic fabrication have been made [11]. The stereolithography based additive manufacturing, including stereolithography apparatus (SLA) and digital light processing (DLP), is based on the controlled light-induced layer-by-layer photopolymerization of a liquid photosensitive resin mixed with ceramic powder [8, 12]. The light engine used in the DLP-stereolithography projects the mask image of sliced layers onto the surface of photosensitive ceramic suspensions, using high performance LEDs as light source and a digital micromirror device (DMD) as dynamic mask, hence it has a higher building speed compared with the SLA-stereolithography and is advantageous for the fabrication of ceramic components with a very good feature resolution [13, 14].

To date, numerous studies have confirmed the viability and effectiveness of the stereolithography to fabricate Al_2O_3 ceramic parts. For instance, the Al_2O_3 ceramic windowpanes with fully dense microstructure were fabricated by M.L. Griffith and J.W. Halloran, who were the first to adopt stereolithography for ceramic freeform fabrication in 1996 [15]. The drying and debinding processes of SLA-stereolithography were optimized by M. Zhou et al., and a defect-free Al_2O_3 cutting tool with a relative density of 99.3% was

obtained [16]. The DLP-stereolithography was used to prepare Al_2O_3 ceramic parts with good surface quality and a relative density of 93.2%, which demonstrated the effectiveness of DLP-stereolithography [11]. Works by O. Santoliquido et al. [17] and X. Shuai et al. [18] have detailed the use of DLP-stereolithography for the fabrication of Al_2O_3 architectures with fine and complex lattice structures. However, it is worth noting that the presence of photosensitive resin in printed green parts and its removal during the debinding process can result in a large porosity in the debound parts [19], which can lengthen the pathways for substance migration at high temperatures and be an obstacle for the sintering densification [20, 21]. For this reason, an increased sintering temperature is required for the debound samples to form dense ceramic parts. The exorbitant high sintering temperature (1550 ~ 1750 °C) of stereolithography-based 3D printed Al_2O_3 ceramics [15, 16, 22-27] is expected to cause the abnormal grain growth and heterogeneous microstructure of Al_2O_3 ceramics. For instance, as presented in Refs. [20] and [24], the grain sizes of the Al_2O_3 ceramics fabricated by stereolithography were 24 and 12 times larger than the average particle sizes of the feedstock Al_2O_3 powders, respectively; In addition, a satisfactory microstructure uniformity of the Al_2O_3 ceramics prepared by SLA-stereolithography can hardly be obtained even if the Al_2O_3 samples were sintered at a relative low temperature (1550 °C) [27]. The abnormal grain growth and non-uniform microstructure can result in lower flexural strength and reliability of ceramics [28, 29], which will further shorten service lifetime of ceramic substrates and heat sinks [30] and thus restrict their application in electronics. Therefore, it is urgent to refine and homogenize the microstructure of Al_2O_3 ceramics prepared by stereolithography-based 3D printing, in order to improve the

flexural strength and reliability of Al_2O_3 ceramics.

The addition of yttria (Y_2O_3), which strongly segregates or precipitates in the form of yttrium aluminates at Al_2O_3 grain boundaries due to its limited solubility (< 10 ppm) in Al_2O_3 crystal lattice [31, 32], is known to inhibit grain growth of Al_2O_3 and represent an effective way for microstructure refinement, through changing the activation energy of grain boundary diffusion and motion [33, 34]. As a result, the mechanical strength of Al_2O_3 or Al_2O_3-based ceramic can be noticeably enhanced [35, 36]. Y_2O_3 is conventionally doped by mechanical mixing (MM) [35], but it is difficult to obtain a homogeneous microstructure, especially a uniform distribution of yttrium aluminates by this method [37]. Compared with the conventional MM process, the chemical precipitation coating (CP) process, which has been employed in the preparation of YAG, SiC and translucent Al_2O_3 ceramics [38-40], shows more homogeneous mixing performance and can improve the microscopic uniformity of ceramics. Furthermore, the dispersive performance of additives (Y_2O_3) in Al_2O_3 matrix is expected to lead to the morphology change of second phases (yttrium aluminates), and the thermal conductivity of ceramics can be highly affected by the grain growth and the morphology of second phases, as commonly seen in AlN ceramic [41, 42]. Nevertheless, this CP process has never been used for the preparation of stereolithography-based 3D printed Al_2O_3 ceramics. To the best of our knowledge, few researches have evaluated the thermal conductivity of stereolithography-based 3D printed Al_2O_3 ceramics, which is significantly essential for thermal management applications of Al_2O_3 ceramics. The effect of the way of introducing additives on the thermal conductivity of Al_2O_3 ceramics has not been investigated so far.

In this study, a CP process was used to fabricate an amorphous Y_2O_3 coating on the surface of Al_2O_3 powder, in order to improve the dispersive homogeneity of Y_2O_3 in Al_2O_3 matrix. The coating effectiveness and integrity were examined in detail by transmission electron microscopy (TEM) and X-ray photoelectron spectroscopy (XPS) measurements. In addition, to demonstrate the advantage of the CP process, the phase transformation, microstructure, thermal and mechanical properties comparisons were made between the CP and conventional MM processed Al_2O_3 samples. The current study shows that, as compared with the conventional MM process, the CP process is a viable approach for refining - homogenizing the microstructure and enhancing the flexural strength - reliability of the DLP-stereolithography based 3D printed Y_2O_3-Al_2O_3 ceramics without decreasing their thermal conductivity.

2 Experimental procedure

2.1 Preparation of Y_2O_3-Al_2O_3 composite powders

Commercially available α-Al_2O_3 powder (D_{50}=200 nm, TM-DAR, Taimei Chemicals Co., Ltd., Japan) was used as starting material. Y_2O_3 additives were used to refine microstructure and enhance mechanical strength of Al_2O_3 ceramics [33, 35, 37]. Two batches of Y_2O_3-Al_2O_3 composite powders were prepared by the CP and MM process, respectively, and both of them had the same content of Y_2O_3. For the conventional MM route, 95 wt% of Al_2O_3 and 5 wt% of Y_2O_3 (D_{50}=500 nm, Shanghai Macklin Biochemical Co., Ltd., China) powders were ball milled in ethanol for 6 h employing a planetary ball mill (QM-QX4, Nanjing NanDa

Instrument Plant, China), with the milling speed set to 250 r/min. The MM system consisted of powders / ethanol / zirconia ball at a weight ratio of 1:3:2 in a Teflon container. After ball-milling, the powders were dried in a rotary evaporator and granulated through a 150 μm sieve. For the CP route, the non-aqueous precursor and precipitant solutions were used for avoiding hard agglomeration of Y_2O_3-coated Al_2O_3 composite powder during drying, and the whole CP process is shown in Fig. 1. Firstly, $Y(NO_3)_3 \cdot 6H_2O$ (99.99% purity, Shanghai Aladdin Bio-Chem Technology Co., Ltd., China) was dissolved in ethanol to prepare the precursor solution, where the concentration of Y^{3+} was accurately controlled to 0.05 mol/L. Secondly, the Al_2O_3 powder was slowly added in the prepared precursor solution, and mixed with 1.5 wt% of dispersants of polyethylene glycol (PEG 2000). The weight ratio of the Y_2O_3 (calculated based on the transformation of $Y(NO_3)_3$ to Y_2O_3) to Al_2O_3 was set to 5:95. Thirdly, the above suspension was dispersed in a bath under ultrasound for 60 min, and then vigorously stirred for 120 min to prevent the sedimentation of ceramic particles. Fourthly, the mixed solution (pH = 12.66) of ethylenediamine (EDA) and ethanol with the weight ratio of 1:2 was prepared as the precipitant solution, and was slowly dropped into the ceramic suspension under strong mechanical stirring to tailor the pH value of the suspension in the range of 9.3~9.5. During the dripping process of the precipitant solution, the precipitations of yttrium-amine complex were formed and simultaneously deposited on the Al_2O_3 powder surface, which can act as the preferential heterogeneous nucleation sites [43]. After the above precipitation coating process, the resultant suspension was continuously stirred for 120 min. Then, the as-prepared composite ceramic powder (Al_2O_3 coated with the yttrium-amine complexes) were washed

with ethanol and air-dried at 60 °C for 10 h. Finally, the dried products were calcined at 450 °C for 2 h to decompose yttrium-amine complexes into Y_2O_3, and the calcined powder was granulated through a 150 μm sieve.

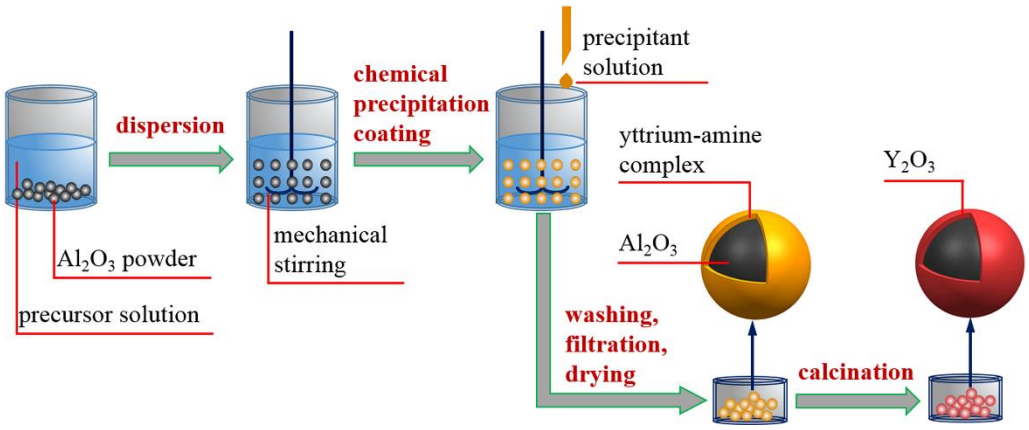

Fig. 1 Schematic illustration of the chemical precipitation coating process.

2.2 Preparation of UV-curable ceramic suspension

Before the preparation of UV-curable ceramic suspensions, the pure Al_2O_3, MM and CP processed Y_2O_3-Al_2O_3 powders were separately surface modified with oleic acid (OA, Shanghai Aladdin Bio-Chem Technology Co., Ltd., China). Firstly, the ceramic powder was dispersed in ethanol, and 1.0 wt% of OA with respect to the mass of ceramic powder was used as surface modifier. The suspension was ball-milled for 2 h employing a planetary ball mill to facilitate physical adsorption of OA on powder surface. Then the suspension was dried at 50 °C for 12 h to remove ethanol and the remaining powder was thermally treated at 80 °C for 6 h to promote chemical adsorption [27, 44]. Finally, the treated ceramic powder was de-agglomerated by passing them through a 150 μm sieve.

The UV-curable ceramic suspension was prepared by adding 79 wt% of above modified

ceramic powder into the photosensitive resin, which was fabricated by mixing ethoxylated pentaerythritol tetraacrylate (PPTTA, Royal DSM, Netherlands), 1,6-hexanediol diacrylate (HDDA, Royal DSM, Netherlands), di-functional aliphatic polyurethane acrylate (U600, Royal DSM, Netherlands), octanol (Shanghai Aladdin Bio-Chem Technology Co., Ltd., China), polyethylene glycol (Shanghai Aladdin Bio-Chem Technology Co., Ltd., China) with commercial dispersant (BYK9077, BYK Additives & Instruments, Germany). The above ceramic suspension was ball-milled for 6 h at 350 r/min using a planetary ball mill. After the ball-milling process, the photoinitiator (Irgacure819, BASF, Germany), with an effective absorption peak range well matched with the wavelength of the UV light used for DLP processing in this study, was mixed into the homogeneous suspension to produce a UV-curable ceramic suspension.

2.3 DLP-stereolithography based 3D printing

3D printing was performed at room temperature by using a DLP-stereolithograpgy based apparatus. The UV light source of the DLP printer is below the vat and has a wavelength of 405 nm with a light intensity of 10.5 mW/cm^2. A 3D model was first created using the UG software and output to a STL file, then the STL file was imported into the stereolithography machine and sliced into 2D images. The Al_2O_3 green bodies were obtained by DLP-stereolithography using the above-mentioned ceramic suspensions. During the DLP-stereolithography process, the UV light selectively cured the photosensitive resin in ceramic suspension based on the 2D images and created cross-linked polymer networks to bond

ceramic particles together. The photopolymerisation process was generally proceeded in a layer-by-layer pattern. The layer thickness was set to 20 μm, and the cure depth was 83.00±2.51 μm by adjusting the exposure time to 3.0 s, giving a high vertical resolution and an adequate integration between layers. Once a single layer was cured, the vat was tilted down to detach the cured layer and the building platform was lifted to allow recoating the suspension layer at the bottom of the vat. Then the new layer was cured subsequently in exactly the same fashion. These steps were repeated until the whole green body was eventually fabricated.

2.4 Debinding and sintering

For printed Al_2O_3 green bodies, the post-processing steps including debinding and sintering were carried out to obtain Al_2O_3 ceramic parts. A two-step debinding process was adopted in this work [16], in which green bodies were firstly debound under vacuum to decelerate pyrolysis rate of resins and then debond in air to completely remove the residual carbon. The debound samples were subsequently sintered in a muffle furnace (HTK 16/18, Thermconcept, Germany) at 10 °C/min from room temperature to 800 °C, then at 5 °C/min up to 1650 °C, with a final plateau of 2 h. Finally the furnace was cooled at 5 °C/min to 800 °C, and then naturally cooled to room temperature. The sintered specimens were machined and polished to evaluate their thermal and mechanical properties. The 3D printed Al_2O_3 ceramics fabricated using the MM and CP processed (i.e., ball-milled and coated) Y_2O_3-Al_2O_3 composite powders are referred to as Sample MM and Sample CP, respectively. In addition, the monolithic Al_2O_3 reference samples prepared by pure Al_2O_3 powder are referred to as

Sample AL.

2.4 Characterization

The microstructure and element analysis of the coated Al_2O_3 powder were investigated by a transmission electron microscopy (TEM, Talos F200S, Thermo Fisher Scientific Inc., America) coupled with an energy dispersive spectroscope (EDS). The TEM sample (coated Al_2O_3 powder) was dispersed in ethanol with ultrasonic treatment and then dropped onto a holey-carbon-coated copper grid. An X-ray photoelectron spectroscopy (XPS, Escalab 250Xi, Thermo Fisher Scientific Inc., America) was used to study the surface chemistry of the MM and CP processed Y_2O_3-Al_2O_3 powders. The contents of Y and Al in the MM and CP processed Y_2O_3-Al_2O_3 powders were determined by an X-ray fluorescence spectrometer (XRF-1800, Shimadzu Co., Ltd., Japan), in order to identify whether both composite powders have the same chemical compositions.

The relative density of the sintered Al_2O_3 ceramic samples was measured by Archimedes method using an analytical balance with an accuracy of 0.0001 g. The bending strength of samples with a size of 1.5 mm × 2.0 mm × 25 mm was evaluated by three-point bending tests [45]. The loading experiments were performed using a universal mechanical testing machine (Inspekt Table Blue 05, Hegewald & Peschke, Germany), with the crosshead speed set to 0.5 mm/min and the supporting span of 20 mm. A laser thermal conductivity instrument (LFA 447, Netzsch Instruments Co., Ltd., Germany) was used to determine the thermal diffusivity (α) of the sintered Al_2O_3 samples with a size of 10 mm × 10 mm × 2 mm at room temperature. The

value of the thermal conductivity (λ) for samples was calculated from:

$$\lambda = \alpha \cdot \rho \cdot C \tag{1}$$

where α is the thermal diffusivity, ρ is the density and C is the specific heat capacity of the prepared samples [46]. In the present work, the thermal conductivity of Sample AL was determined by taking the specific heat capacity value of the high purity Al_2O_3 ceramics (0.755 $J \cdot g^{-1} \cdot K^{-1}$ at room temperature) [47]. Y_2O_3 doping can result in the formation of a second phase (yttrium aluminum garnet, YAG) in Al_2O_3 ceramic [37], and the specific heat capacities of the Y_2O_3-Al_2O_3 system (Samples MM and CP) were calculated by using the Neumann-Kopp rule [48]:

$$C = \sum_{i=1}^{n} \omega_i C_i \tag{2}$$

where ω_i is the mass fraction of each phase which can be determined by XRD analysis, and C_i is the corresponding specific heat capacity for the constituents (Al_2O_3 and YAG). A documented value of 0.60 $J \cdot g^{-1} \cdot K^{-1}$ is used for the specific heat capacity of YAG [49, 50].

The phase composition of the sintered samples was determined by X-ray diffraction (XRD, D8 Advance, Bruker Corporation, Germany). A scanning range of 2θ from 10 ° to 80 ° was applied. The mass percentage of the phases in the sintered sample was also semiquantitatively estimated by analyzing the reference intensity ratio (RIR) value taken from the X-ray pattern [51]. The weight fraction of phase 1 in the sintered ceramics can be calculated from:

$$X_1 = \frac{I_1}{RIR_1} \cdot \frac{1}{\sum_{i=1}^{n} \left(I_i / RIR_i \right)} \tag{3}$$

where X_1 is the weight fraction of phase 1, I_i is the integrated intensity of the highest peak of the *i*th phase in the analyzed ceramic, RIR_i is the reference intensity ratio of the *i*th phase (taken from the powder diffraction database), and *n* is the number of phases in the prepared ceramics.

To identify the fracture surface features and global distribution profile of Y element throughout the 3D printed samples, the images of fracture surface and the corresponding X-ray mapping analysis of Y element were studied by a scanning electron microscopy (SEM, LYRA 3 XMU, Tescan, Czech) coupled with an energy-dispersive spectroscopy (EDS, Inca X-Max50, Oxford Instruments, England). Moreover, the prepared samples were polished with diamond paste and then thermally etched at 1550 °C for 30 min. The microstructures of the polished and fracture surface of the sintered ceramics were characterized by the scanning electron microscopy. The average grain size was determined by the Nanomeasure software, and at least 600 grain sizes were statistically analyzed for each sample. The Christiansen uniformity coefficient (*CU*) was used to quantitatively determine the distribution uniformity of the grain size in the sintered ceramics, which can be calculated using the following equations [52]:

$$CU = 1 - \sum_{i=1}^{n} \frac{\left| x_i - \bar{x} \right|}{n\bar{x}} \tag{4}$$

where $\bar{x}$ is the average grain size, which can be calculated by $\bar{x} = \frac{1}{n}\sum_{i=1}^{n} x_i$, x_i is the size of the *i*th grain, *n* is the total number of grains, *CU* is the Christiansen uniformity coefficient, and the larger *CU* value indicates the more uniform microstructure of sintered ceramic.

3 Results and Discussion

3.1 Characterization of CP processed Al_2O_3 powder

The weight percent of Y/(Y+Al) of the MM and CP processed Y_2O_3-Al_2O_3 composite powders were measured to be 7.12 wt% and 7.40 wt%, respectively, by an XRF spectrometer, indicating that the composite powders prepared by MM and CP processes have nearly the same Y_2O_3 content. The microstructure of the CP processed composite powder was analyzed. TEM results of the CP processed Y_2O_3-Al_2O_3 powder are presented in Fig. 2. The morphology of the CP processed Y_2O_3-Al_2O_3 powder is shown in Fig. 2a, which displays that an evident shell layer was closely, uniformly attached to the Al_2O_3 particle surface. From a high resolution image as shown in Fig. 2b, the CP processed Y_2O_3-Al_2O_3 powder has a typical core-shell structure with a relatively smooth surface layer, which is about ~2.31 nm thick. According to a further fast Fourier transform (FFT) pattern analysis, the dispersive diffraction halo in Fig. 2c shows that the shell is amorphous; and Fig. 2d presents the lattice fringes of Al_2O_3 (2-13) and (-114) planes with interplanar spacing of about 0.201 nm and 0.259 nm, respectively, indicating that the core is Al_2O_3 crystalline. This result verifies that a uniform amorphous deposition was formed on the surface of the Al_2O_3 particle. To check the element compositions of the amorphous layer, the EDS analyses were conducted on both amorphous layer (shell) and the bulk of the Al_2O_3 particle (core), shown in Fig. 2e and 2f, respectively. The major elements in shell are Al, Y, O with minor C and Cu, meanwhile, only Al, O, C and Cu peaks can be detected in the core. The C and Cu elements come from the holey-carbon-coated copper grid used in the TEM sample preparation. This EDS result indicates that the chemical

composition of the shell is Y-O compound. The TEM and EDS results suggest that the Al_2O_3 particle is encapsulated by the amorphous layer of Y-O compound.

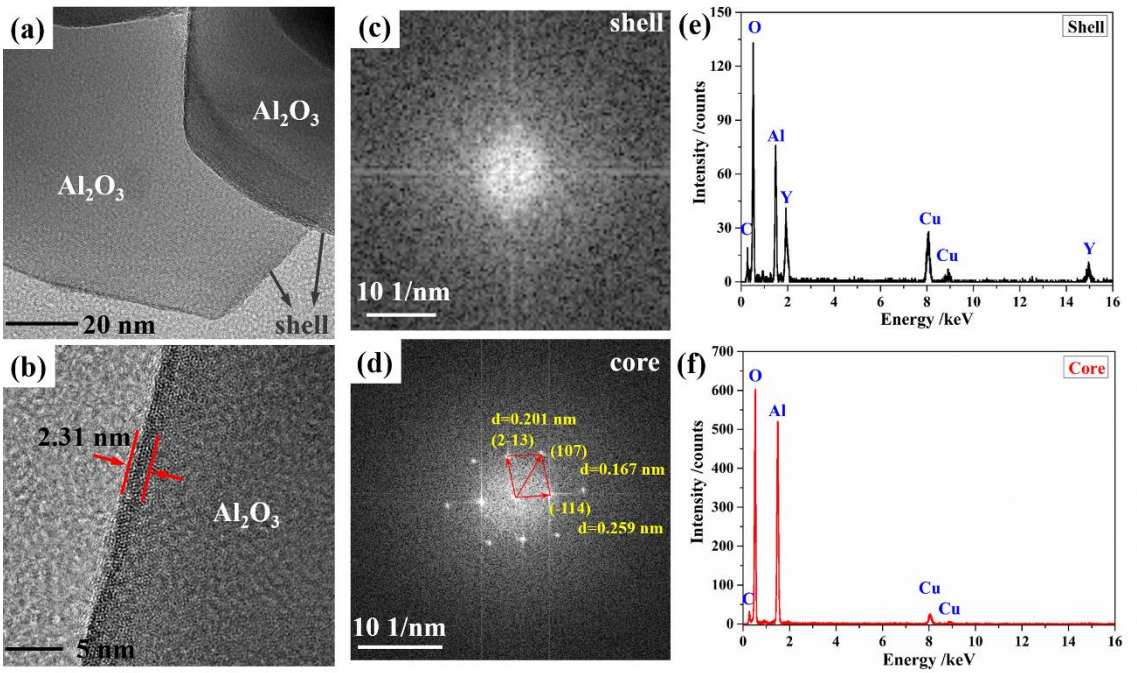

Fig. 2 (a) Representative TEM image of the CP processed Y_2O_3-Al_2O_3 ceramic powder, (b) high magnification TEM image representing the surface of the CP processed powder, (c) and (d) are the corresponding fast Fourier transform patterns of the shell and core, (e) and (f) are respective EDS spectra recorded from the shell and core.

The XRD patterns for the MM and CP processed Y_2O_3-Al_2O_3 composite powders are shown in Fig. 3. The diffraction peaks of the MM processed composite powder can be identified as phases of α-Al_2O_3 and cubic Y_2O_3, indicating that the MM processed powder is a mixture of α-Al_2O_3 and Y_2O_3 powders. However, the XRD pattern of the CP processed composite powder only shows sharp diffraction peaks assigned to α-Al_2O_3, and a very broad peak of Y_2O_3 is present at 29.15 ° (which is the diffraction angle of the strongest diffraction peak of Y_2O_3), implying that the Y_2O_3 in the CP processed composite powder is amorphous.

This result is consistent with the TEM observation and corresponding FFT pattern of the amorphous shell of the coated Al_2O_3 powder (Figs. 2b and 2c).

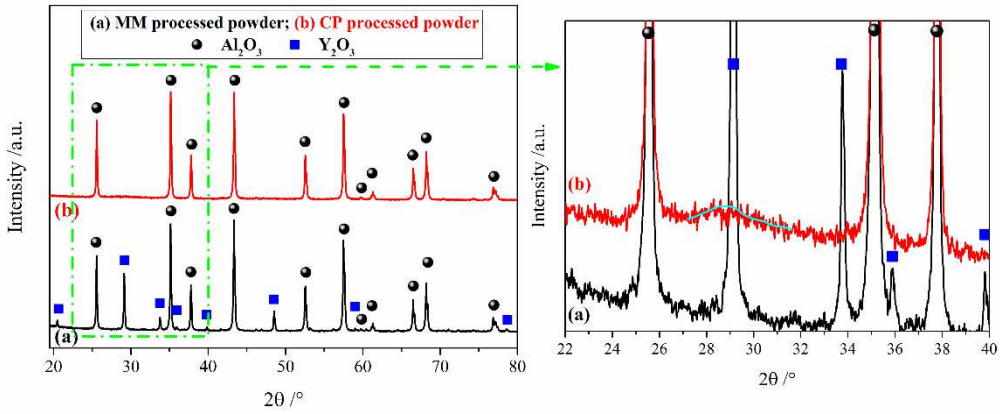

Fig. 3 XRD patterns for the MM and CP processed Y_2O_3-Al_2O_3 composite powders. Right image is the local enlargement of left image marked by green box.

To examine the elements present and their chemical states on the ceramic powder surface, the XPS measurements of the MM and CP processed Y_2O_3-Al_2O_3 composite powders were carried out. The XPS survey scan and narrow scans of Y_{3d} are shown in Fig. 4, and the binding energies of the obtained peaks are referenced to the C_{1s} signal for C-H. Both the spectra of the MM and CP processed Y_2O_3-Al_2O_3 powders reveal the peaks for O_{1s}, Y_{3d} and Al_{2p}, which indicates the presence of O, Y and Al, as shown in Fig. 4a. Figs. 4b and 4c show the narrow scan for Y_{3d} core level, and the raw data was fitted using the Thermo Advantage V5.52 software. The high-resolution Y_{3d} spectrum (Figs. 4b and 4c) can be decomposed into couple of doublets related to the spin-orbit splitting of $Y_{3d\ 5/2}$ and $Y_{3d\ 3/2}$. The $Y_{3d\ 5/2}$ peaks locate at 157.96 eV and 157.55 eV for the CP and MM processed Y_2O_3-Al_2O_3 powders, respectively. These $Y_{3d\ 5/2}$ binding energies are in accordance with the documented values (158.1 eV and

157.4 eV) for $Y_{3d\ 5/2}$ of Y_2O_3 [53, 54], so the $Y_{3d\ 5/2}$ in the CP processed Y_2O_3-Al_2O_3 powders can be assigned to Y^{3+} in Y_2O_3. The quantitative calculations from the narrow scan results of Al_{2p}, O_{1s}, C_{1s} and Y_{3d} were performed to determine the chemical compositions of the MM and CP processed Y_2O_3-Al_2O_3 powders, as shown in Table 1. The Y/Al atomic ratio of the CP processed Y_2O_3-Al_2O_3 powder is calculated to be 0.2081, which is much greater than the Y/Al atomic ratio of the MM processed Y_2O_3-Al_2O_3 powder (0.0023) and stoichiometric mixture (95 wt% Al_2O_3 + 5 wt% Y_2O_3) (0.0238). The much higher value of the Y/Al atomic ratio in the CP processed Y_2O_3-Al_2O_3 powder can evidence that the surface of the CP processed Al_2O_3 powder is enriched with Y, i.e., Y is localized in the surface layer of the CP processed Al_2O_3 powder [55]. It can be concluded from the TEM, XRD and XPS results that the surface of the Al_2O_3 ceramic powder is covered with an amorphous Y_2O_3 layer prepared by the CP process.

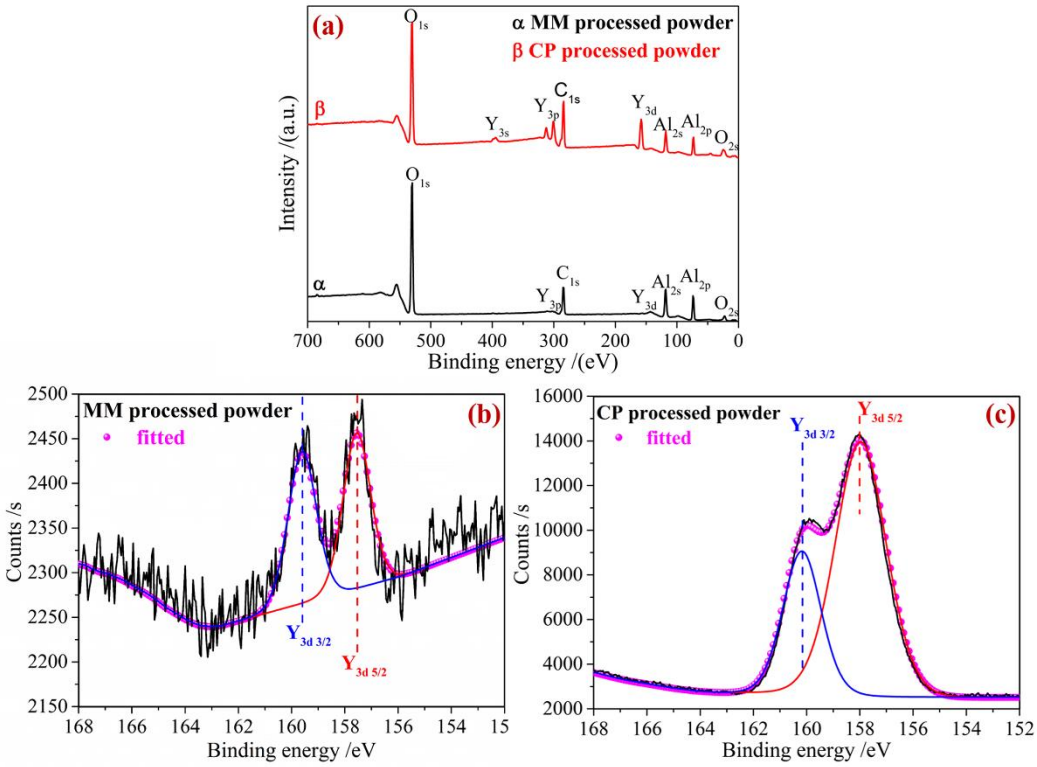

Fig. 4 (a) XPS survey scan of the MM and CP processed Y_2O_3-Al_2O_3 powders; (b) and

(c) respective XPS core level spectra of Y_{3d} in the MM and CP processed Y_2O_3-Al_2O_3 powders.

Table 1 Chemical compositions (at%) of the MM and CP processed Y_2O_3-Al_2O_3 powders

Sample	C_{1s}	O_{1s}	Al_{2p}	Y_{3d}
MM processed Y_2O_3-Al_2O_3 powder	24.88	44.76	30.29	0.07
CP processed Y_2O_3-Al_2O_3 powder	36.62	39.52	19.75	4.11

3.2 Phase analysis and microstructure of sintered Al_2O_3 ceramics

The XRD patterns of the 3D printed Al_2O_3 ceramic samples are shown in Fig. 5, and the peak intensities are normalized relative to the Al_2O_3 (211). Diffraction peaks of α-Al_2O_3, as the only phase for Sample AL, are exhibited in Fig. 5 (a). The XRD patterns of Samples MM and CP show α-Al_2O_3 and $Y_3Al_5O_{12}$ (YAG) as the primary and minor phase, respectively. With the addition of Y_2O_3 into Al_2O_3, the YAG phase is generated by a series of reactions as follows [56, 57]:

$$Al_2O_3 + 2\ Y_2O_3 = Y_4Al_2O_9 \quad (5)$$

$$Y_4Al_2O_9 + Al_2O_3 = 4\ YAlO_3 \quad (6)$$

$$3YAlO_3 + Al_2O_3 = Y_3Al_5O_{12} \quad (7)$$

Combining the above reaction equations, a simplified expression can be obtained:

$$5\ Al_2O_3 + 3\ Y_2O_3 = 2\ Y_3Al_5O_{12} \quad (8)$$

Based on the Eq. (8), 5 wt% of Y_2O_3 can react with 3.76 wt% Al_2O_3 to form $Y_3Al_5O_{12}$ in the 5 wt% Y_2O_3 - 95 wt% Al_2O_3 system, thus the theoretical mass percentages of $Y_3Al_5O_{12}$

and Al_2O_3 in the sintered ceramic are calculated to be 8.76 wt% and 91.24 wt%, respectively. The content of each phase in the prepared ceramic samples was estimated by the RIR analysis from the X-ray diffraction data and the result is listed in Table 2. It can be seen that the contents of $Y_3Al_5O_{12}$ in Samples MM and CP are 8.16 wt% and 8.74 wt%, respectively, which are basically coincident with the theoretical calculation value. This result indicates that the Y_2O_3 had been completely reacted with Al_2O_3 in Samples MM and CP by high temperature sintering. Moreover, the calculated mass fraction of each phase can be used to determine the specific heat capacities of Samples MM and CP via the Eq. (2).

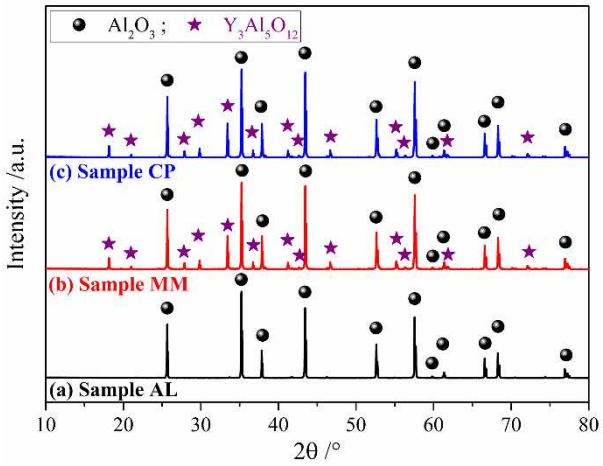

Fig. 5 XRD patterns for the prepared Al_2O_3 ceramic samples.

Table 2 Phase content in the prepared Al_2O_3 ceramics estimated by the semi-quantitative method

Sample	Semi-quantitative phase content in ceramics /wt%		Semi-quantitative phase content in ceramics /vol%	
	Al_2O_3	$Y_3Al_5O_{12}$	Al_2O_3	$Y_3Al_5O_{12}$
AL	100.00	0	100.00	0
MM	91.84	8.16	92.79	7.21
CP	91.26	8.74	92.27	7.73

Figure 6 demonstrates the SEM observation on the microstructures of different sintered Al_2O_3 samples and their grain size distributions. In this figure, the white zone at grain boundary areas corresponds to the $Y_3Al_5O_{12}$ second phase (as shown in Fig. 5), while the gray and black sections are Al_2O_3 grains and pores, respectively. Compared with Sample AL (Fig. 6a), Samples MM and CP (Figs. 6b and 6c) possess higher porosities, corresponding to the relatively higher density of Samples AL as shown in Table 3. It suggests that the densification of Al_2O_3 matrix was slightly inhibited by the addition of 5 wt% of Y_2O_3. On the one hand, the yttrium segregation at Al_2O_3/Al_2O_3 interfaces can block the diffusion of ions along grain boundaries, leading to a reduced grain boundary diffusivity and hence a decreased densification rate [33, 34, 58]. On the other hand, once above the Y_2O_3 solubility-limit in Al_2O_3, the extra Y_2O_3 would react with Al_2O_3 matrix and then form $Y_3Al_5O_{12}$ precipitations via the solid state reactions (Eqs. 5 ~ 7). The $Y_3Al_5O_{12}$ precipitations, present at grain boundaries and multigrain junctions in Al_2O_3 matrix, can result in Zener pinning action on grain boundary mobility and finally retarding the densification of Al_2O_3 matrix [59, 60].

As shown in Fig. 6a, the 3D printed monolithic Al_2O_3 ceramic possesses an obvious coarsening and inhomogeneous microstructure (grain size up to 4.78 μm, and with a low Christiansen uniformity coefficient of 0.50). The introduction of Y_2O_3 enables the Al_2O_3 matrix grain size to be refined, due to the pinning effect of $Y_3Al_5O_{12}$ precipitations [33, 59]. The mean grain sizes of Samples MM and CP are smaller than that in Sample AL by 26.78% and 64.44%, respectively. Furthermore, the grain size of Sample CP (~ 1.70 μm) is 51.43%

smaller than that of Sample MM (~ 3.50 μm). It suggests that the different introducing ways of Y_2O_3 would result in different growth trends for the Al_2O_3 grains. Compared to Sample MM, Sample CP shows much refined $Y_3Al_5O_{12}$ precipitations and an increased degree of $Y_3Al_5O_{12}$ distribution range at grain boundary areas in the matrix. This precipitation feature displayed in Samples CP can lead to more areas of Zener pinning on grain boundary migration, and hence enable a much refined and homogenous Al_2O_3 matrix microstructure. By way of illustration, in both Ref. [24] and present work, the same Al_2O_3 powder was used; although the sintering temperature (1600 °C) in Ref. [24] is lower than that (1650 °C) in the present work, the grain size of Sample CP is much less than the value reported in that work (2.6 μm) [24]. The microstructure refinement is often expected to fabricate Al_2O_3 ceramic with higher strength according to the Hall-Petch relationship [61]. Furthermore, Sample CP has the narrowest grain size distribution, with a Christiansen uniformity coefficient of 0.70, which is 12.90% and 40.00% higher than those of Samples MM and AL, respectively. This finding demonstrates that the CP process can make the microstructure of Al_2O_3 ceramic more uniform, which can play a crucial role in improving the reliability of Al_2O_3 ceramics.

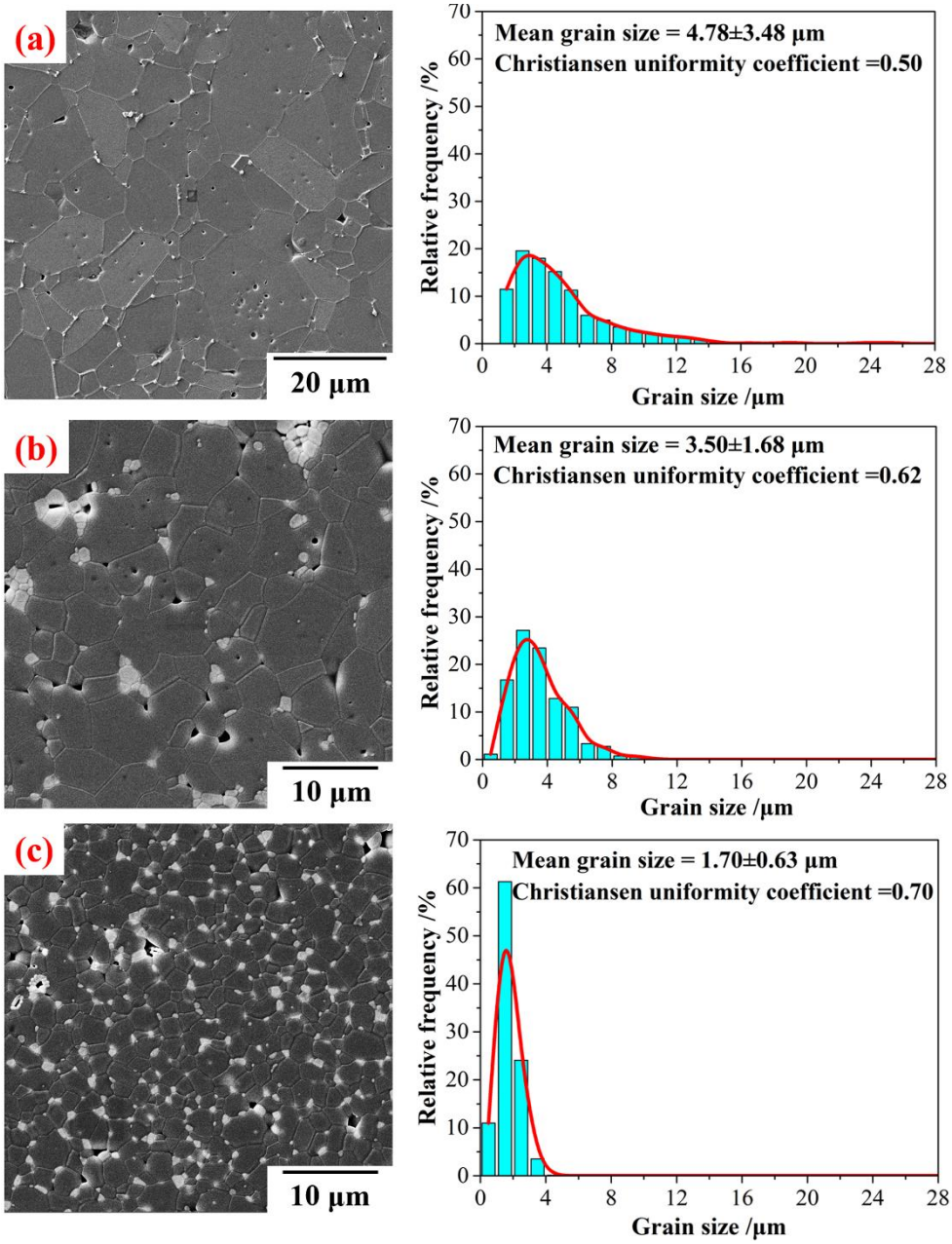

Fig. 6 Microstructures and grain size statistics of (a) Sample AL, (b) Sample MM and (c) Sample CP.

3.3 Properties of 3D printed Al_2O_3 ceramics

The mechanical and thermal properties of the 3D printed Al_2O_3 ceramics are listed in Table 3. The relative density of pure Al_2O_3 ceramic (Sample AL) is higher than those of Y_2O_3-

Al_2O_3 system (Samples MM and CP), demonstrating that the addition of 5 wt% of Y_2O_3 is detrimental for the densification of Al_2O_3 ceramic. In addition, Sample CP has a higher relative density than Sample MM, which is consistent with the denser microstructure of Sample CP (Fig. 6c) compared to that of Sample MM (Fig. 6b), illustrating that the CP process can improve the relative density of the Y_2O_3-Al_2O_3 system compared with the conventional MM process.

Table 3 Mechanical and thermal properties of the 3D printed Al_2O_3 ceramics

Sample	Relative density /%	Flexural strength /MPa	Thermal conductivity / $W \cdot m^{-1} \cdot K^{-1}$
AL	98.19±0.12	362.98±28.61	33.40±1.51
MM	97.31±0.23	396.50±46.84	29.16±0.55
CP	97.53±0.15	455.37±32.17	28.95±0.28

As displayed in Table 3, Sample AL has the lowest flexural strength, which is 8.45% and 20.29% lower than those of Samples MM and CP, respectively, i.e., the addition of Y_2O_3 is favorable to the improvement of flexural strength of the 3D printed Al_2O_3 ceramic. The improved flexural strength of the Y_2O_3-Al_2O_3 system is resulted from the fine grain strengthening and dispersion strengthening of the $Y_3Al_5O_{12}$ particles [62, 63]. The flexural strength of Sample CP is 14.85% higher than that of Sample MM, owing to the finer Al_2O_3 grain and more homogeneous microstructure of Sample CP (as shown in Fig. 6c); also the relative density improvement can lead to an increase in flexural strength of Sample CP, according to the empirical suggestion for the strength of ceramics [1]. Fracture surface SEM micrographs of the 3D printed ceramic samples are shown in Fig. 7. Fractures predominantly

occurred in an intergranular mode for Samples AL and MM (Figs. 7a and 7b). On the other hand, a large proportion of Al_2O_3 grains fractured transgranularly in Sample CP (Fig. 7c). This indicates that the Al_2O_3 grain boundaries in Sample CP should be much stronger than those in Samples AL and MM, leading to the increased flexural strength for Sample CP.

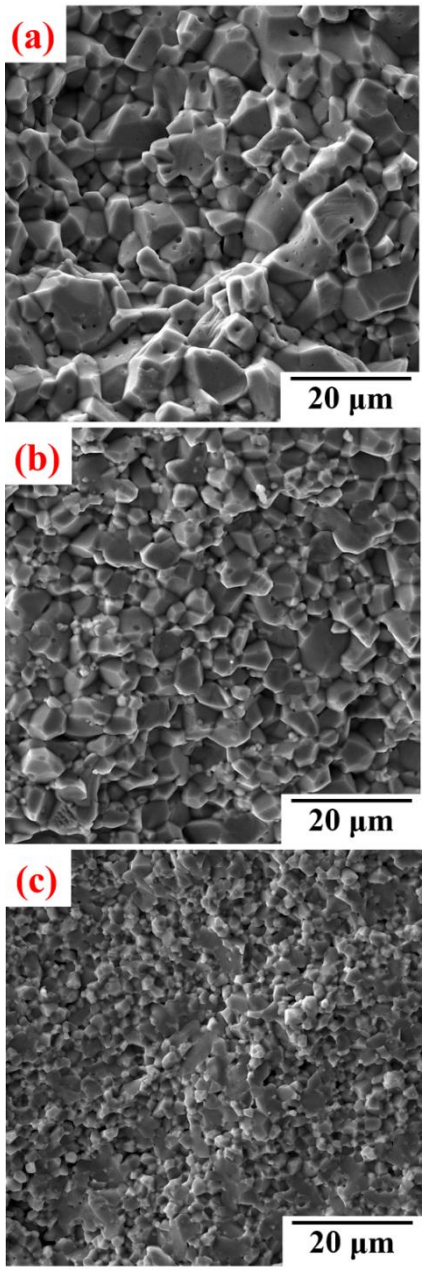

Fig. 7 SEM micrographs of the fracture surfaces of (a) Sample AL, (b) Sample MM and (c) Sample CP.

Furthermore, reliability analysis was conducted by estimating the Weibull modulus of the flexural strength distribution using at least 16 samples [64]. The two-parameter Weibull distribution was calculated by the equation:

$$\ln\ln\left(\frac{1}{1-P_f}\right) = m\ln\sigma_n - m\ln\sigma_0 \quad (9)$$

where P_f=(n-0.5)/N is an estimator of the fracture probability of the nth ranked sample, n is the rank of the bending strength data, N is the total number of samples tested (N = 16 in the present work), m is the Weibull modulus, σ_n is the measured bending strength and σ_0 is the Weibull material scale parameter [64]. A higher m value means a better uniformity of flexural strength and a higher reliability of ceramic. The flexural strength distribution of Samples AL, MM and CP is shown in Fig. 8. The Weibull modulus for Sample MM is 35.33% lower than that for Sample AL, illustrating that the introduction of Y_2O_3 into Al_2O_3 via the conventional MM process can decrease the reliability of Al_2O_3 ceramic. The agglomeration of $Y_3Al_5O_{12}$ second (as shown in Fig. 6b) can make the homogeneity of Sample MM deterioration, thus leading the reduction of Weibull modulus. Compared to the Weibull modulus for Sample MM, a very drastic increase from 9.59 to 16.88 in the Weibull modulus for Sample CP was obtained, indicating a much higher reliability and repeatability. These above findings illustrate that the CP process is beneficial to simultaneously enhance the flexural strength and reliability of the 3D printed Al_2O_3 ceramic.

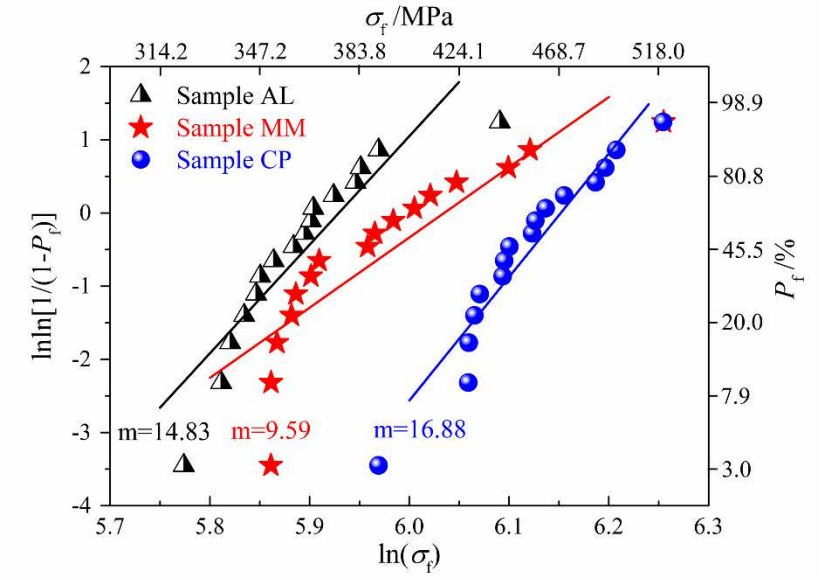

Fig. 8 Weibull plots for the flexural strength of Samples AL, MM and CP.

It can be seen from Table 3 that the thermal conductivity of pure Al_2O_3 ceramic (Sample AL) is 14.54% and 15.37% higher than those of Samples MM and CP (Y_2O_3-Al_2O_3 system), respectively. The addition of 5 wt% of Y_2O_3 causes a fall in thermal conductivity compared with that of pure Al_2O_3 and this is accompanied by the decreased relative density and formation of second phase ($Y_3Al_5O_{12}$). The pores and second phases can enhance phonon scattering and decrease the effective conductive mean free path, therefor reduce the thermal conductivity according to the kinetic theory of phonons in solids [65, 66]. Based on the Maxwell model, the thermal conductivity of ceramic sample with isolated pores dispersed in a ceramic matrix is written as [67]:

$$\lambda = \lambda_0 \cdot \frac{2(1-\varphi)}{2+\varphi} \tag{10}$$

where λ is the apparent thermal conductivity of ceramic with pores, φ is the porosity of ceramic and φ = 1- *RD*% (relative density), and λ_0 is the thermal conductivity of completely

dense ceramic without pore (φ = 0). By substituting the measured thermal conductivity and relative density of Sample AL into Eq. (10), the thermal conductivity of the dense Al_2O_3 ceramic is calculated to be 34.32 $W \cdot m^{-1} \cdot K^{-1}$, which is in accordance with the documental values (33±2 $W \cdot m^{-1} \cdot K^{-1}$,) for pure dense Al_2O_3 at ambient temperature [47]. From the mathematical analysis by Eq. (10), the increase of porosity can result in a drop in thermal conductivity. Thus the Y_2O_3-Al_2O_3 system with lower relative density has a thermal conductivity inferior to the denser pure Al_2O_3 ceramic.

The component and structure of composite material has a significant effect on the thermal conductivity [68]. For Y_2O_3-Al_2O_3 composite system (Al_2O_3 ceramic with a small amount of $Y_3Al_5O_{12}$ second phase), the Maxwell-Eucken (ME) model can be used to predict the thermal conductivity via the following relation [69-71]:

$$\lambda_c = \lambda_s \cdot \frac{2\lambda_s + \lambda_p + 2V_p(\lambda_p - \lambda_s)}{2\lambda_s + \lambda_p - V_p(\lambda_p - \lambda_s)} \tag{11}$$

where λ_c , λ_s and λ_p are the thermal conductivities of the composite ceramic, Al_2O_3 and $Y_3Al_5O_{12}$ phase, respectively, and V_p is the volume fraction of $Y_3Al_5O_{12}$ phase. In the present work, a value of λ_p = 10.7 $W \cdot m^{-1} \cdot K^{-1}$ was used for the thermal conductivity of pure $Y_3Al_5O_{12}$ phase [72], which is much lower than the thermal conductivity of dense Al_2O_3 ceramic (34.32 $W \cdot m^{-1} \cdot K^{-1}$). If the morphology of second phase is not completely isolated, the effect of the connectivity of second phase on the thermal conductivity of composite system cannot be ignored. An appropriate model is given by the effective medium theory (EMT), and the thermal conductivity of composite system is given by [69, 73]:

$$\lambda_c = \frac{1}{4}\left\{\lambda_p(3V_p - 1) + \lambda_s(2 - 3V_p) + [(3\lambda_p V_p - \lambda_p + 2\lambda_s - 3\lambda_s V_p)^2 + 8\lambda_p\lambda_s]^{\frac{1}{2}}\right\} \quad (12)$$

The calculated thermal conductivities derived from Eqs. (10), (11) and (12) are shown in Table 4. The formation of $Y_3Al_5O_{12}$ precipitations with a low thermal conductivity can result in a drop in thermal conductivity of Y_2O_3-Al_2O_3 system based on the ME and EMT model analyses. However, the thermal conductivities of Y_2O_3-Al_2O_3 system estimated by the ME and EMT models are higher than the measured values of thermal conductivities of Samples MM and CP since the phonon scattering caused by the pores, second phase precipitations and grain boundaries can decrease the phonon mean free path and further lead to the reduction of thermal conductivity [66, 69]. Thus, the addition of Y_2O_3 into Al_2O_3 is expected to reduce the thermal conductivity of 3D printed Al_2O_3 ceramic.

Table 4 A comparison between the calculated and measured thermal conductivities of Y_2O_3-Al_2O_3 system

Calculation model	Sample	λ_s	λ_p	λ_{c0}	φ	$\lambda_{c\text{-calculated}}$	$\lambda_{c\text{-measured}}$
ME	MM	34.32	10.70	32.16	2.69%	30.88	29.16
	CP	34.32	10.70	32.00	2.47%	30.83	28.95
EMT	MM	34.32	10.70	32.13	2.69%	30.85	29.16
	CP	34.32	10.70	31.97	2.47%	30.80	28.95

The grain boundaries can act as the scattering sites for phonons and reduce the thermal conductivity of ceramic [69]. This reduction can be enhanced by decreasing the grain size, which is attributed to the increased number of grain boundaries per unit length of heat path. However, compared to the coarse grained Sample MM, the fine grained Sample CP has a

similar value of thermal conductivity, rather than a lower value, as shown in Table 3, because the thermal conductivity of ceramic is also highly affected by second phase morphology [42]. The SEM image and corresponding EDS mapping for Y on the fracture surfaces of Sample MM sintered at 1650 °C are shown in Figs. 9a1 and 9a2. Sample MM has large Y patches distributed heterogeneously (Fig. 9a2), and these patches are on the average size of 2.85±1.24 μm, which is comparable to the grain size of Sample MM (3.50±1.68 μm), manifesting an apparent agglomeration of $Y_3Al_5O_{12}$ phase during sintering. A presence of semi-connected $Y_3Al_5O_{12}$ aggregates can be observed in Fig. 9a3, and the $Y_3Al_5O_{12}$ aggregates distributes continuously along Al_2O_3 grain boundaries in Sample MM. The second phased distribution of Sample CP sintered at 1650 °C is shown in Figs. 9b1 ~ 9b3. Sample CP has small Y patches distributed homogeneously (Fig. 9b2), and these patches are on the average size of 0.71±0.26 μm, which is much lower than the grain size of Sample CP (1.70±0.63 μm); Combined with the results obtained from SEM micrograph of Sample CP (Fig. 6c), the small-sized $Y_3Al_5O_{12}$ particles tend to be concentrated at multigrain junctions without continuous distribution along Al_2O_3 grain boundaries. The morphologic change of the second phase from semi-connected (Sample MM) to isolated (Sample CP) can contribute to an improvement of the thermal conductivity of Al_2O_3 ceramics, according to the comparison between EMT model (Eq. 12) for the interconnected second phase and ME model (Eq. 11) for the isolated second phase [42, 68]. In addition, compared to Sample MM, the higher relative density of Sample CP can lead to an increase in thermal conductivity. From all the above analysis, Sample CP has a close thermal conductivity to Sample MM due to the combined contribution of grain size, second

phase morphology and relative density.

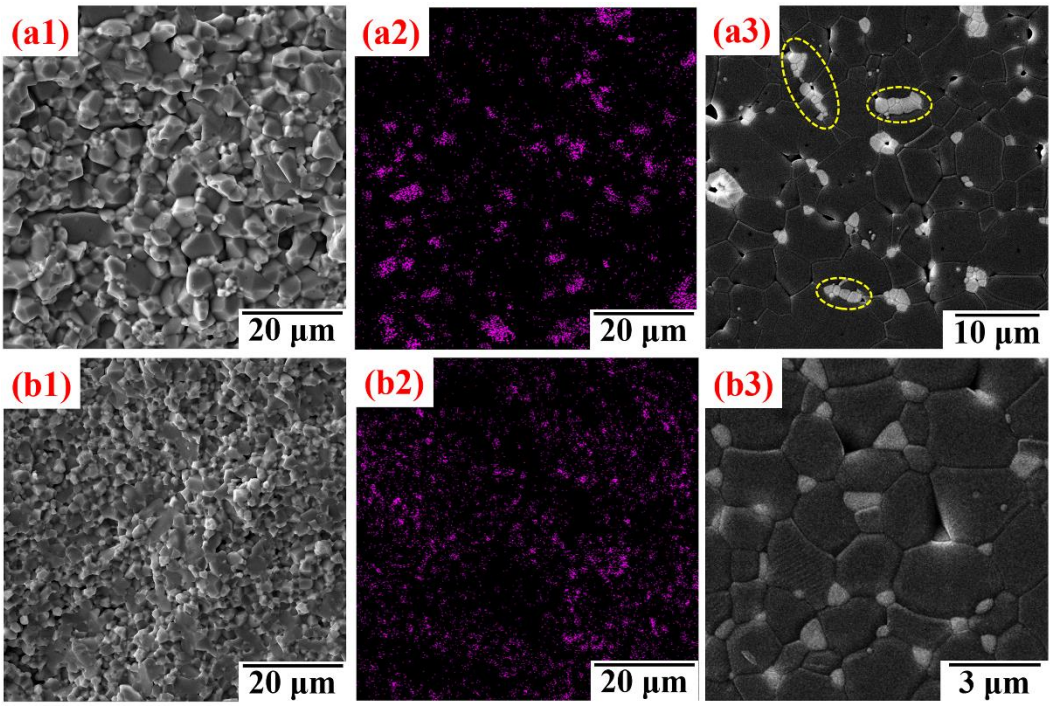

Fig. 9 SEM images and corresponding EDS mappings for Y on the fracture surfaces of Sample MM (a1, a2) and Sample CP (b1, b2); SEM micrographs of the polished and etched surfaces of Sample MM (a3) and Sample CP (b3). The semi-connected second phases are marked with red circles.

According to the above research results, the CP process is an effective method to enhance the flexural strength and reliability of 3D printed Al_2O_3 ceramic. Typical Al_2O_3 ceramic components with complex shapes can be fabricated by a novel approach integrating DLP-stereolithography and CP process, as shown in Fig. 10. The surface smoothness of the fabricated parts appears to be fine. The pin-type heat sinks with different fin configuration are shown in Fig. 10, which shows potential application in thermal management in electronics and automotive industries [74]. Therefore, the fundamental study of this paper can offer an alternative approach to fabricate ceramic heat sinks with complex shapes and excellent

mechanical performance.

Fig. 10 Optical image of fin-type Al_2O_3 ceramic heat sinks fabricated by a novel approach integrating DLP-stereolithography and CP process.

4 Conclusion

In this study, a special Al_2O_3 ceramic with complex shape, high strength, and fine grained and homogeneous microstructure was successfully fabricated by a novel approach integrating DLP-stereolithography and chemical precipitation coating (CP) process. The CP process was used to synthetize Y_2O_3-coated Al_2O_3 composite powder, which was then used to print complex-shaped Al_2O_3 bodies via DLP-stereolithography. It was found that:

(1) The microstructure, phase and surface element present analyses for the CP processed Al_2O_3 powder clearly demonstrates that an amorphous Y_2O_3 layer can be fully wrapped on the surface of Al_2O_3 powder, which will be favorable for improving the dispersive homogeneity of Y_2O_3 in Al_2O_3.

(2) The phase and microstructure comparisons among the 3D printed Al_2O_3 samples prepared via the pure Al_2O_3 powder (AL), CP, and mechanical mixing (MM) processed Y_2O_3-

Al_2O_3 powders shows: i) the introduction of Y_2O_3 into Al_2O_3 can result in the generation of $Y_3Al_5O_{12}$ phase precipitations, which can reduce the grain size of Al_2O_3 due to the precipitation pinning; ii) compared to the conventional MM process, the CP process can make the microstructure of the 3D printed Y_2O_3-Al_2O_3 system denser, more uniform and refined.

(3) Sample CP has a flexural strength of 455.37±32.17 MPa and a Weibull modulus of 16.88, which are 15.10% and 76.02% higher than those obtained for Sample MM, due to the grain refinement and microstructure uniformity enhancement. In addition, Sample CP has much higher flexural strength and Weibull modulus compared to Sample AL, indicating the CP process is conductive to simultaneously improving the flexural strength and reliability of the 3D printed Al_2O_3 ceramic.

(4) The CP process can refine the microstructure of Y_2O_3-Al_2O_3 system at no expense of the thermal conductivity. The fine grained Sample CP has a close thermal conductivity (28.95±0.28 $W \cdot m^{-1} \cdot K^{-1}$) to the coarse grained Sample MM (29.16±0.55 $W \cdot m^{-1} \cdot K^{-1}$), because the CP process can facilitate the formation of $Y_3Al_5O_{12}$ phase as isolated pockets at corners of Al_2O_3 grains, which can benefit the decrease of phonon scattering caused by the second phase.

(5) Some fin-type Al_2O_3 ceramic heat sinks were successfully fabricated via the CP process followed by DLP-stereolithography, which may offer a new opportunity for thermal management applications of Al_2O_3 ceramic.

Acknowledgement

This work was supported by the Local Innovative and Research Team Project of

Guangdong Province (Grant No. 2017BT01C169), the Opening Project of State Key Laboratory of Green Building Materials (Grant No. 2019GBM03), the Guangdong Basic and Applied Basic Research Foundation (Grant No. 2020A1515010004), the Natural Science Foundation of Guangdong Province (Grant No. 2018A030313353), and the Science and Technology Program of Guangzhou (Grant No. 201904010357).

References

[1] Ge R, Zhang Y, Liu YJ, *et al*. Effect of Gd_2O_3 addition on mechanical, thermal and shielding properties of Al_2O_3 ceramics. *J Mater Sci: Mater Electron* 2017, **28**: 5898-5905.

[2] Dong GC, Chen X, Zhang XJ, *et al*. Thermal fatigue behaviour of Al_2O_3-DBC substrates under high temperature cyclic loading. *Solder Surf Mt Tech* 2010, **22**: 43-48.

[3] Santos WND, Filho PIP, Taylor R. Effect of addition of niobium oxide on the thermal conductivity of alumina. *J Eur Ceram Soc* 1998, **18**: 807-811.

[4] Wu H, Liu W, Lin L, *et al*. Preparation of alumina-toughened zirconia via 3D printing and liquid precursor infiltration: manipulation of the microstructure, the mechanical properties and the low temperature aging behavior. *J Mater Sci* 2019, **54**: 7447-7459.

[5] Baklouti S, Bouaziz J, Chartier T, *et al*. Binder burnout and evolution of the mechanical strength of dry-pressed ceramics containing poly(vinyl alcohol). *J Eur Ceram Soc* 2001, **21**: 1087-1092.

[6] Xie R, Zhang D, Zhang X, *et al*. Gelcasting of alumina ceramics with improved green strength. *Ceram Int* 2012, **38**: 6923-6926.

[7] Liu W, Xie Z. Pressureless sintering behavior of injection molded alumina ceramics. *Sci Sinter* 2014, **46**: 3-13.

[8] He R, Liu W, Wu Z, *et al*. Fabrication of complex-shaped zirconia ceramic parts via a DLP-stereolithography-based 3D printing method. *Ceram Int* 2018, **44**: 3412-3416.

[9] Wu H, Liu W, He R, *et al*. Fabrication of dense zirconia-toughened alumina ceramics through a stereolithography-based additive manufacturing. *Ceram Int* 2017, **43**: 968-972.

[10] Singh S, Ramakrishna S, Singh R. Material issues in additive manufacturing: A review. *J Manuf Process* 2017, **25**: 185-200.

[11] Song X, Chen Y, Lee TW, *et al*. Ceramic fabrication using mask-image-projection-based stereolithography integrated with tape-casting. *J Manuf Process* 2015, **20**: 456-464.

[12] Komissarenko DA, Sokolov PS, Evstigneeva AD, *et al*. Rheological and curing behavior of acrylate-based suspensions for the DLP 3D printing of complex zirconia parts. *Materials* 2018, **11**: 2350.

[13] Chen Z, Li Z, Li J, *et al*. 3D printing of ceramics: A review. *J Eur Ceram Soc* 2019, **39**: 661-687.

[14] Felzmann R, Gruber S, Mitteramskogler G, *et al*. Lithography-based additive manufacturing of cellular ceramic structures. *Adv Eng Mater* 2012, **14**: 1-7.

[15] Griffith ML, Halloran JW. Freeform fabrication of ceramics via stereolithography. *J Am Ceram Soc* 1996, **79**: 2601-2608.

[16] Zhou M, Liu W, Wu H, *et al*. Preparation of a defect-free alumina cutting tool via additive manufacturing based on stereolithography - optimization of the drying and debinding

processes. *Ceram Int* 2016, **42**: 11598–11602.

[17] Santoliquido O, Colombo P, Ortona A. Additive manufacturing of ceramic components by digital light processing: A comparison between the "bottom-up" and the "top-down" approaches. *J Eur Ceram Soc* 2019, **39**: 2140-2148.

[18] Shuai X, Zeng Y, Li P, *et al*. Fabrication of fine and complex lattice structure Al_2O_3 ceramic by digital light processing 3D printing technology. *J Mater Sci* 2020, **55**: 6771-6782.

[19] Li H, Liu Y, Liu Y, *et al*. Influence of vacuum debinding temperature on microstructure and mechanical properties of three-dimensional-printed alumina via stereolithography. *3D Print Addit Manuf* 2020, **7**: 8-18.

[20] An D, Li H, Xie Z, *et al*. Additive manufacturing and characterization of complex Al_2O_3 parts based on a novel stereolithography method. *Int J Appl Ceram Tec* 2017, **14**: 836-844.

[21] An D, Liu W, Xie Z, *et al*. A strategy for defects healing in 3D printed ceramic compact via cold isostatic pressing: sintering kinetic window and microstructure evolution. *J Am Ceram Soc* 2019, **102**: 2263-2671.

[22] Zhang S, Sha N, Zhao Z. Surface modification of α-Al_2O_3 with dicarboxylic acids for the preparation of UV-curable ceramic suspensions. *J Eur Ceram Soc* 2017, **37**: 1607–1616.

[23] Schwentenwein M, Homa J. Additive manufacturing of dense alumina ceramics. *Int J Appl Ceram Tec* 2015, **12**: 1-7.

[24] Liu W, Wu H, Tian Z, *et al*. 3D printing of dense structural ceramic microcomponents

with low cost: Tailoring the sintering kinetics and the microstructure evolution. *J Am Ceram Soc* 2019, **102**: 2257-2262.

[25] Chartier T, Chaput C, Doreau F, *et al*. Stereolithography of structural complex ceramic parts. *J Mater Sci* 2002, **37**: 3141-3147.

[26] Wu H, Cheng Y, Liu W, *et al*. Effect of the particle size and the debinding process on the density of alumina ceramics fabricated by 3D printing based on stereolithography. *Ceram Int* 2016, **42**: 17290-17294.

[27] Li K, Zhao Z. The effect of the surfactants on the formulation of UV-curable SLA alumina suspension. *Ceram Int* 2017, **43**: 4761-4767.

[28] Deng L, Qiao L, Zheng J, *et al*. Injection molding, debinding and sintering of ZrO_2 ceramic modified by silane couping agent. *J Eur Ceram Soc* 2020, **40**: 1566–1573.

[29] Ai YL, Xie XH, He W, *et al*. Effect of nano-Al_2O_3 on the microstructure and properties of ZrO_2 dental materials prepared by microwave sintering. *Appl Mech Mater* 2014, **618**: 3-7.

[30] Miyazakia H, Iwakiri S, Hirao K, *et al*. Effect of high temperature cycling on both crack formation in ceramics and delamination of copper layers in silicon nitride active metal brazing substrates. *Ceram Int* 2017, **43**: 5080-5088.

[31] Mccune RC, Donlon WT, Ku RC. Yttrium segregation and YAG precipitation at surfaces of yttrium-doped α-Al_2O_3. *J Am Ceram Soc* 1986, **69**: 196-199.

[32] Moya EG, Moya F, Lesage B, *et al*. Yttrium diffusion in α-alumina single crystal. *J Eur Ceram Soc* 1998, **18**: 591-594.

[33] Galusek D, Ghillányová K, Sedlácek J, *et al*. The influence of additives on microstrucutre of sub-micron alumina ceramics prepared by two-stage sintering. *J Eur Ceram Soc* 2012, **32**: 1965-1970.

[34] Maca K, Pouchlý V, Bodišová K, *et al*. Densification of fine-grained alumina ceramics doped by magnesia, yttria and zirconia evaluated by two different sintering models. *J Eur Ceram Soc* 2014, **34**: 4363-4372.

[35] Wang R, Zhang D, Zhuang OY, *et al*. Effect of Y_2O_3 content on the properties of alumina-based ceramic cores. *Appl Mech Mater* 2014, **488-489**: 145-149.

[36] Song IG, Kim JS. Enhancement of the mechanical properties of alumina ceramics by a granulation process and Y_2O_3 additive. *Korean J Met Mater* 2015, **53**: 262-269.

[37] Wang H, Gao L, Shen Z, *et al*. Mechanical properties and microstructures of Al_2O_3-5 vol.% YAG composites. *J Eur Ceram Soc* 2001, **21**: 779-783.

[38] Sang Y, Qin H, Liu H, *et al*. Partial wet route for YAG powders synthesis leading to transparent ceramic: A core-shell solid-state reaction process. *J Eur Ceram Soc* 2013, **33**: 2617-2623.

[39] Liu Y, Liu R, Liu M. Improved sintering ability of SiC ceramics from SiC@Al_2O_3 core-shell nanoparticles prepared by a slow precipitation method. *Ceram Int* 2019, **45**: 8032-8036.

[40] Liu W, Xie ZP, Liu GW, *et al*. Novel preparation of translucent alumina ceramics induced by doping additives via chemical precipitation method. *J Am Ceram Soc* 2011, **94**: 3211-3215.

[41] He X, Ye F, Liu LM, *et al*. Microstructure and thermal conductivity of spark plasma sintering AlN ceramics. *Mater Sci Tech* 2011, **27**: 513-517.

[42] Lee HM, Bharathi K, Kim DK. Processing and characterization of aluminum nitride ceramics for high thermal conductivity. *Adv Eng Mater* 2014, **16**: 655-669.

[43] Wang W, Xie Z, Liu G, *et al*. Fabrication of blue-colored zirconia ceramics via heterogeneous nucleation method. *Cryst Growth Des* 2009, **9**: 4373-4377.

[44] Lin L, Wu H, Xu Y, *et al*. Fabrication of dense aluminum nitride ceramics via digital light processing-based stereolithography. *Mater Chem Phys* 2020, **249**: 122969.

[45] ASTM C1161-13, Standard test method for flexural strength of advanced ceramics at ambient temperature, United States: ASTM International, 2013.

[46] ASTM E1461-13, Standard test method for thermal diffusivity by the flash method, United States: ASTM International, 2013.

[47] Munro RG. Evaluated material properties for a sintered α-alumina. *J Am Ceram Soc* 1997, **80**: 1919-1928.

[48] Santos WND, Filho PIP, Taylor R. Effect of addition of niobium oxide on the thermal conductivity of alumina. *J Eur Ceram Soc* 1998, **18**: 807-811.

[49] Kuwano Y, Suda K, Ishizawa N, *et al*. Crystal growth and properties of $(Lu,Y)_3Al_5O_{12}$. *J Cryst Growth* 2004, **260**: 159-165.

[50] Aggarwal RL, Ripin DJ, Ochoa JR, *et al*. Measurement of thermo-optic properties of $Y_3Al_5O_{12}$, $Lu_3Al_5O_{12}$, $YAlO_3$, $LiYF_4$, $LiLuF_4$, BaY_2F_8, $KGd(WO_4)_2$, and $KY(WO_4)_2$ laser crystals in the 80-300K temperature range. *J Appl Phys* 2005, **98**: 103514.

[51] Zhu HB, Li H, Li ZX. Plasma sprayed TiB_2-Ni cermet coatings: Effect of feedstock characteristics on the microstructure and tribological performance. *Surf Coat Tech* 2013, **235**: 620-627.

[52] Chen G, Wan J, He N, *et al*. Strengthening mechanisms based on reinforcement distribution uniformity for particle reinforced aluminum matrix composites. *Trans Nonferrous Met Soc China* 2018, **28**: 2395-2400.

[53] Hayoz J, Bovet M, Pillo T, *et al*. Oxygen-segregation-controlled epitaxy of Y_2O_3 films on Nb(110). *Appl Phys A: Mater Sci Process* 2000, **71**: 615-618.

[54] Barreca D, Battiston GA, Berto D, *et al*. Y_2O_3 thin films characterized by XPS. *Surf Sci Spectra* 2001, **8**: 234-239.

[55] Kosova N, Devyatkina E, Slobodyuk A, *et al*. Surface chemistry study of $LiCoO_2$ coated with alumina. *Solid State Ion* 2008, **179**: 1745-1749.

[56] Matsubara I, Paranthaman M, Allison SW, *et al*. Preparation of Cr-doped $Y_3Al_5O_{12}$ phosphors by heterogeneous precipitation methods and their luminescent properties. *Mater Res Bull* 2000, **35**: 217-224.

[57] Zhao D, Coyle TW, Chien K. Phase composition and microstructure of yttrium aluminum garnet (YAG) coatings prepared by suspension plasma spraying of Y_2O_3-Al_2O_3 powders. *Surf Coat Technol* 2013, **235**: 303-309.

[58] Fang J, Thompson AM, Harmer MP, *et al*. Effect of yttrium and lanthanum on the final-stage sintering behavior of ultrahigh-purity alumina. *J Am Ceram Soc* 1997, **80**: 2005-2012.

[59] Lach R, Wojteczko K, Dudek A, *et al*. Fracture behaviour of alumina-YAG particulate composites. *J Eur Ceram Soc* 2014, **34**: 3373-3378.

[60] Sommer F, Kern F, El-Maghraby HF, *et al*. Effect of preparation route on the properties of slip-casted Al_2O_3/YAG composites. *Ceram Int* 2012, **38**: 4819-4826.

[61] Hansen N. Hall-Petch relation and boundary strengthening. *Scr Mater* 2004, **51**: 801-806.

[62] Armstrong RW. Grain size dependent alumina fracture mechanics stress intensity. *Int J Refract Hard Met* 2001, **19**: 251-255.

[63] Liu L, Maeda K, Onda T, *et al*. Microstructure and improved mechanical properties of Al_2O_3/Ba-β-Al_2O_3/ZrO_2 composites with YSZ addition. *J Eur Ceram Soc* 2018, **38**: 5113-5121.

[64] ISO 20501:2019(E), Fine ceramics (advanced ceramics, advanced technical ceramics) - Weibull statistics for strength data, Switzerland: International Organization for Standardization, 2019.

[65] Negahdari Z, Willert-Porada M, Scherm F. Thermal properties of homogenous lanthanum hexaaluminate/alumina composite ceramics. *J Eur Ceram Soc* 2010, **30**: 3103-3109.

[66] Watari K, Hwang HJ, Toriyama M, *et al*. Effective sintering aids for low-temperature sintering of AlN ceramics, *J Mater Res* 1999, **14**: 1409-1417.

[67] Sumirat I, Ando Y, Shimamura S. Theoretical consideration of the effect of porosity on thermal conductivity of porous materials. *J Porous Mater* 2006, **13**: 439-443.

[68] Carson JK, Lovatt SJ, Tanner DJ, *et al*. An analysis of the influence of material

structure on the effective thermal conductivity of theoretical porous materials using finite element simulations. *Int J Refrig* 2003, **26**: 873-880.

[69] Smith DS, Fayette S, Grandjean S, *et al*. Thermal resistance of grain boundaries in alumina ceramics and refractories. *J Am Ceram Soc* 2003, **86**: 105-111.

[70] Hsu HC, Tuan WH. Thermal characteristics of a two-phase composite. *Adv Powder Technol* 2016, **27**: 929-934.

[71] Boey F, Tok AIY, Lam YC, *et al*. On the effects of secondary phase on thermal conductivity of AlN ceramic substrates using a microstructural modeling approach. *Mater Sci Eng A* 2002, **335**: 281-289.

[72] Hostaša J, Nečina V, Uhlířová T, *et al*. Effect of rare earth ions doping on the thermal properties of YAG transparent ceramics. *J Eur Ceram Soc* 2019, **39**: 53-58.

[73] Kultayeva S, Ha JH, Malik R, *et al*. Effects of porosity on electrical and thermal conductivities of porous SiC ceramics. *J Eur Ceram Soc* 2020, 40: 996-1004.

[74] Onbattuvelli V, Atre S. Review of net shape fabrication of thermally conducting ceramics. *Mater Manuf Process* 2011, **26**: 832-845.

Figure Captions

Fig. 1 Schematic illustration of the chemical precipitation coating process.

Fig. 2 (a) Representative TEM image of the CP processed Y_2O_3-Al_2O_3 ceramic powder, (b) high magnification TEM image representing the surface of the CP processed powder, (c)

and (d) are the corresponding fast Fourier transform patterns of the shell and core, (e) and (f) are respective EDS spectra recorded from the shell and core.

Fig. 3 XRD patterns for the MM and CP processed Y_2O_3-Al_2O_3 composite powders. Right image is the local enlargement of left image marked by green box.

Fig. 4 (a) XPS survey scan of the MM and CP processed Y_2O_3-Al_2O_3 powders; (b) and (c) respective XPS core level spectra of Y_{3d} in the MM and CP processed Y_2O_3-Al_2O_3 powders.

Fig. 5 XRD patterns for the prepared Al_2O_3 ceramic samples.

Fig. 6 Microstructures and grain size statistics of (a) Sample AL, (b) Sample MM and (c) Sample CP.

Fig. 7 SEM micrographs of the fracture surfaces of (a) Sample AL, (b) Sample MM and (c) Sample CP.

Fig. 8 Weibull plots for the flexural strength of Samples AL, MM and CP.

Fig. 9 SEM images and corresponding EDS mappings for Y on the fracture surfaces of Sample MM (a1, a2) and Sample CP (b1, b2); SEM micrographs of the polished and etched surfaces of Sample MM (a3) and Sample CP (b3). The semi-connected second phases are marked with red circles.

Fig. 10 Optical image of fin-type Al_2O_3 ceramic heat sinks fabricated by a novel approach integrating DLP-stereolithography and CP process.

Tables

Table 1 Chemical compositions (at%) of the MM and CP processed Y_2O_3-Al_2O_3 powders

Sample	C_{1s}	O_{1s}	Al_{2p}	Y_{3d}
MM processed Y_2O_3-Al_2O_3 powder	24.88	44.76	30.29	0.07
CP processed Y_2O_3-Al_2O_3 powder	36.62	39.52	19.75	4.11

Table 2 Phase content in the prepared Al_2O_3 ceramics estimated by the semi-quantitative method

Sample	Semi-quantitative phase content in ceramics /wt%		Semi-quantitative phase content in ceramics /vol%	
	Al_2O_3	$Y_3Al_5O_{12}$	Al_2O_3	$Y_3Al_5O_{12}$
AL	100.00	0	100.00	0
MM	91.84	8.16	92.79	7.21
CP	91.26	8.74	92.27	7.73

Table 3 Mechanical and thermal properties of the 3D printed Al_2O_3 ceramics

Sample	Relative density /%	Flexural strength /MPa	Thermal conductivity / $W \cdot m^{-1} \cdot K^{-1}$
AL	98.19±0.12	362.98±28.61	33.40±1.51
MM	97.31±0.23	396.50±46.84	29.16±0.55
CP	97.53±0.15	455.37±32.17	28.95±0.28

Table 4 A comparison between the calculated and measured thermal conductivities of Y_2O_3-Al_2O_3 system

Calculation model	Sample	λ_s	λ_p	λ_{c0}	φ	$\lambda_{c\text{-calculated}}$	$\lambda_{c\text{-measured}}$
ME	MM	34.32	10.70	32.16	2.69%	30.88	29.16
	CP	34.32	10.70	32.00	2.47%	30.83	28.95
EMT	MM	34.32	10.70	32.13	2.69%	30.85	29.16
	CP	34.32	10.70	31.97	2.47%	30.80	28.95

Figures

Figure 1

Schematic illustration of the chemical precipitation coating process.

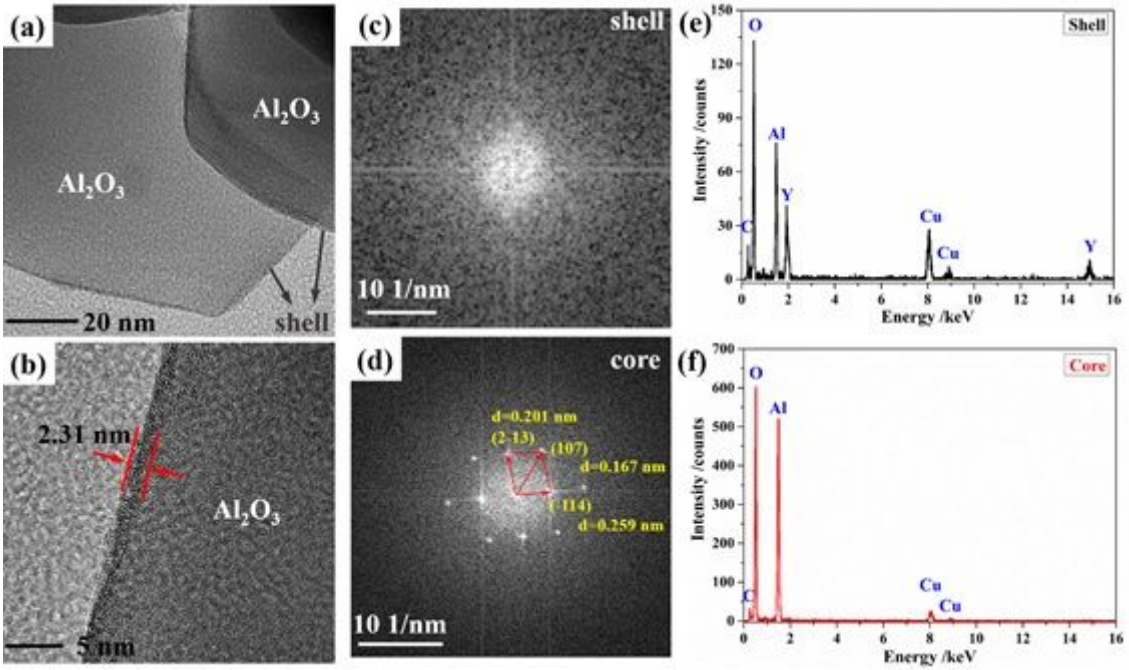

Figure 2

(a) Representative TEM image of the CP processed Y2O3-Al2O3 ceramic powder, (b) high magnification TEM image representing the surface of the CP processed powder, (c) and (d) are the corresponding fast Fourier transform patterns of the shell and core, (e) and (f) are respective EDS spectra recorded from the shell and core.

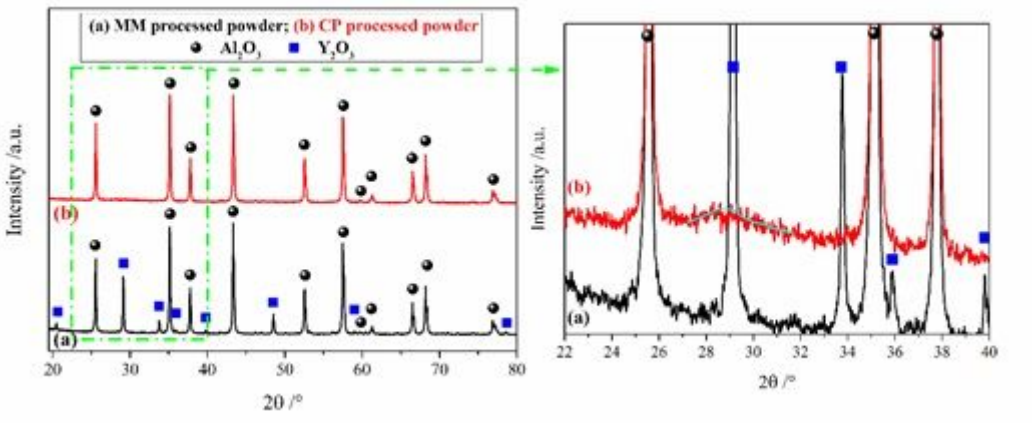

Figure 3

XRD patterns for the MM and CP processed Y2O3-Al2O3 composite powders. Right image is the local enlargement of left image marked by green box.

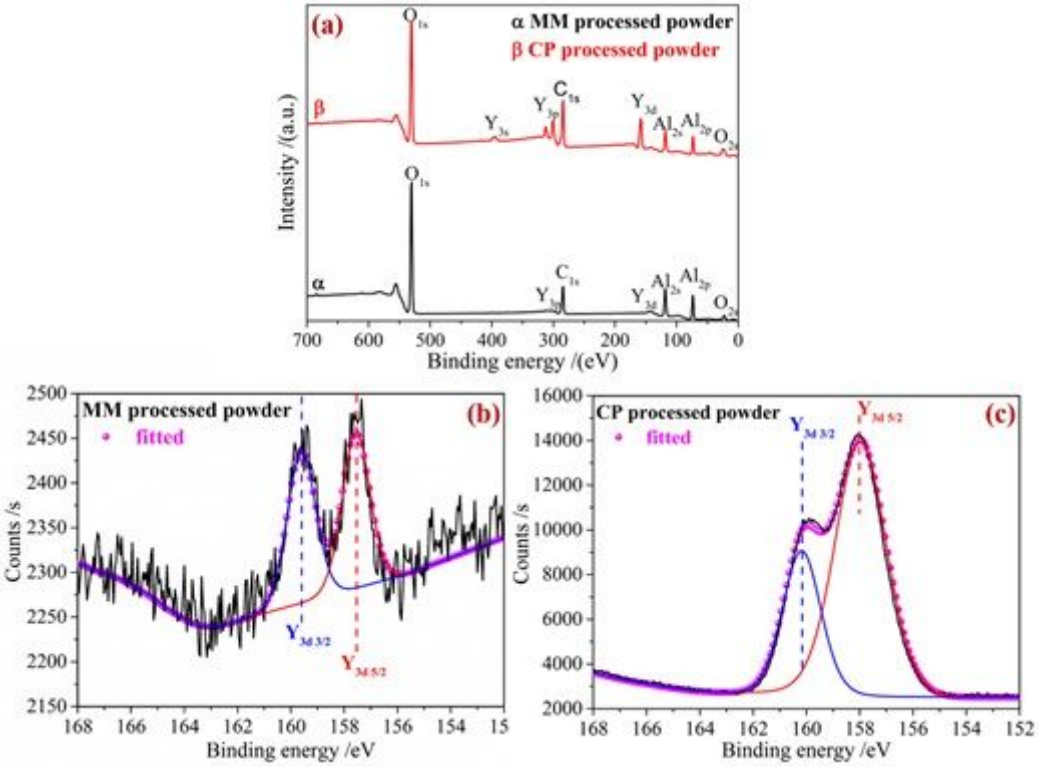

Figure 4

(a) XPS survey scan of the MM and CP processed Y2O3-Al2O3 powders; (b) and (c) respective XPS core level spectra of Y3d in the MM and CP processed Y2O3-Al2O3 powders.

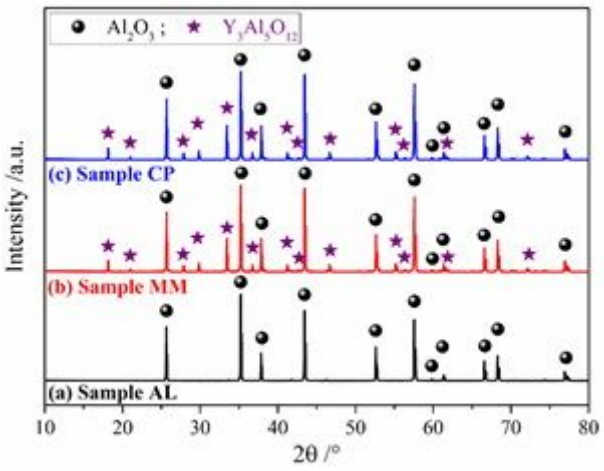

Figure 5

XRD patterns for the prepared Al2O3 ceramic samples.

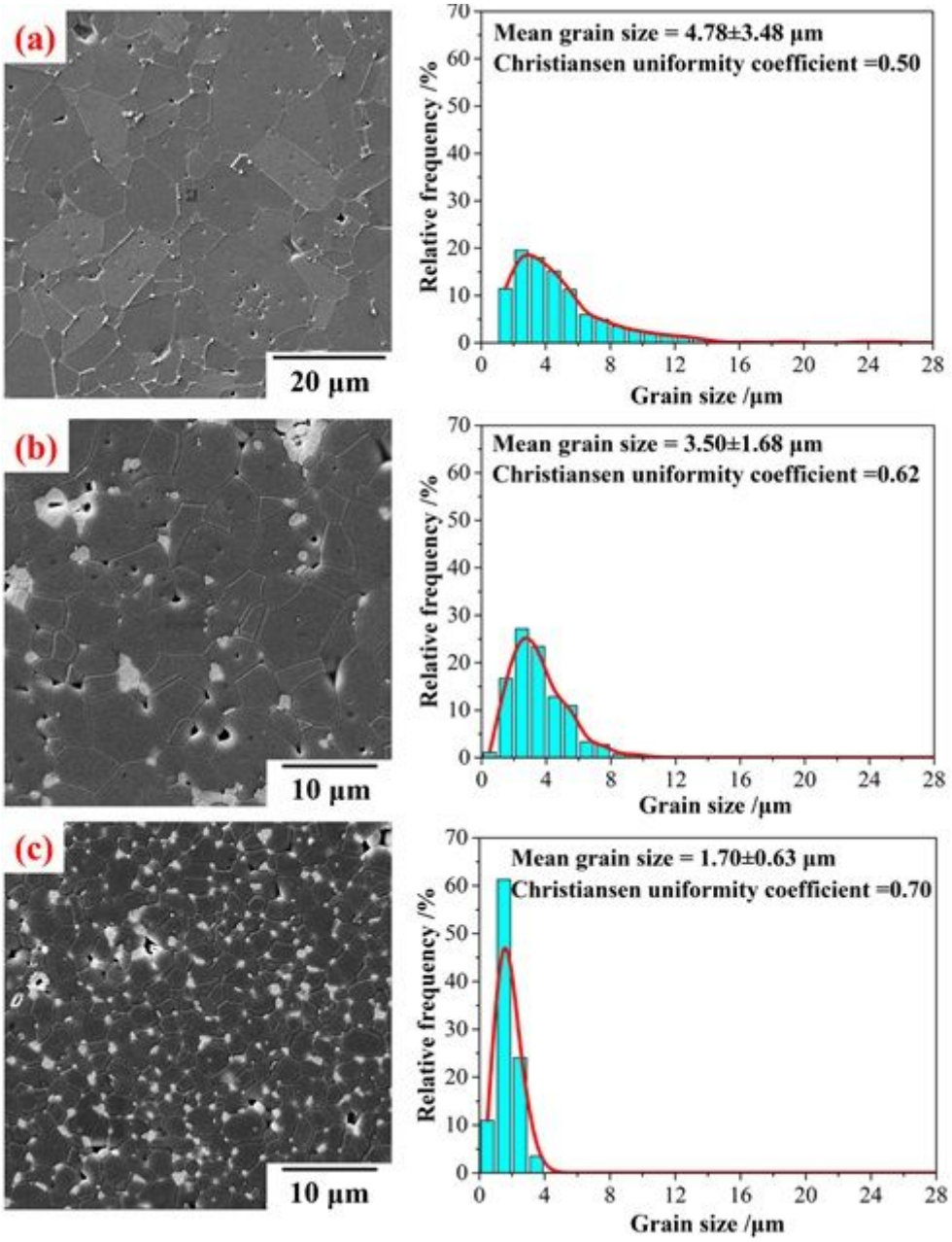

Figure 6

Microstructures and grain size statistics of (a) Sample AL, (b) Sample MM and (c) Sample CP.

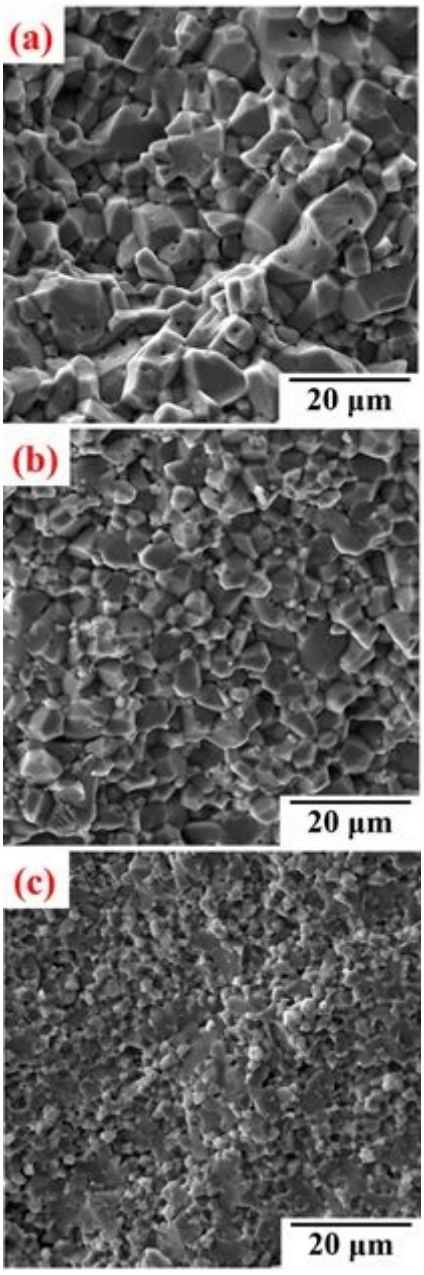

Figure 7

SEM micrographs of the fracture surfaces of (a) Sample AL, (b) Sample MM and (c) Sample CP.

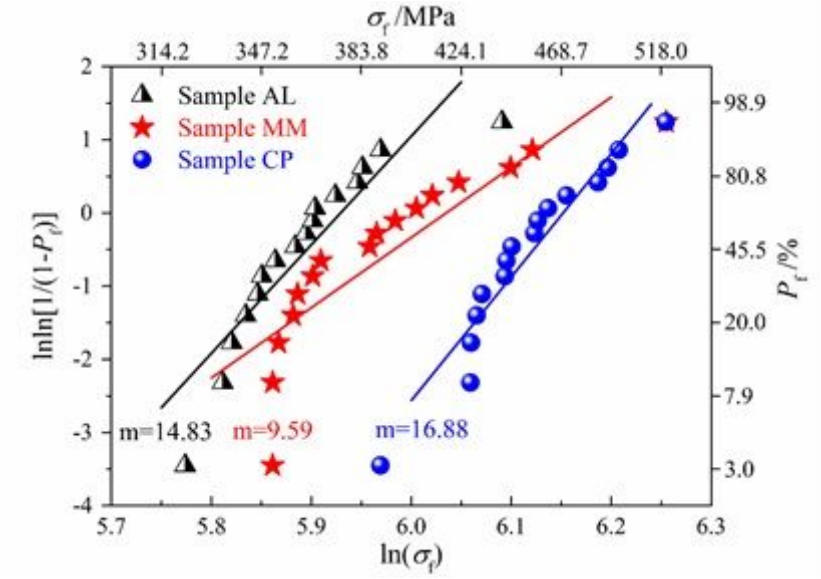

Figure 8

Weibull plots for the flexural strength of Samples AL, MM and CP.

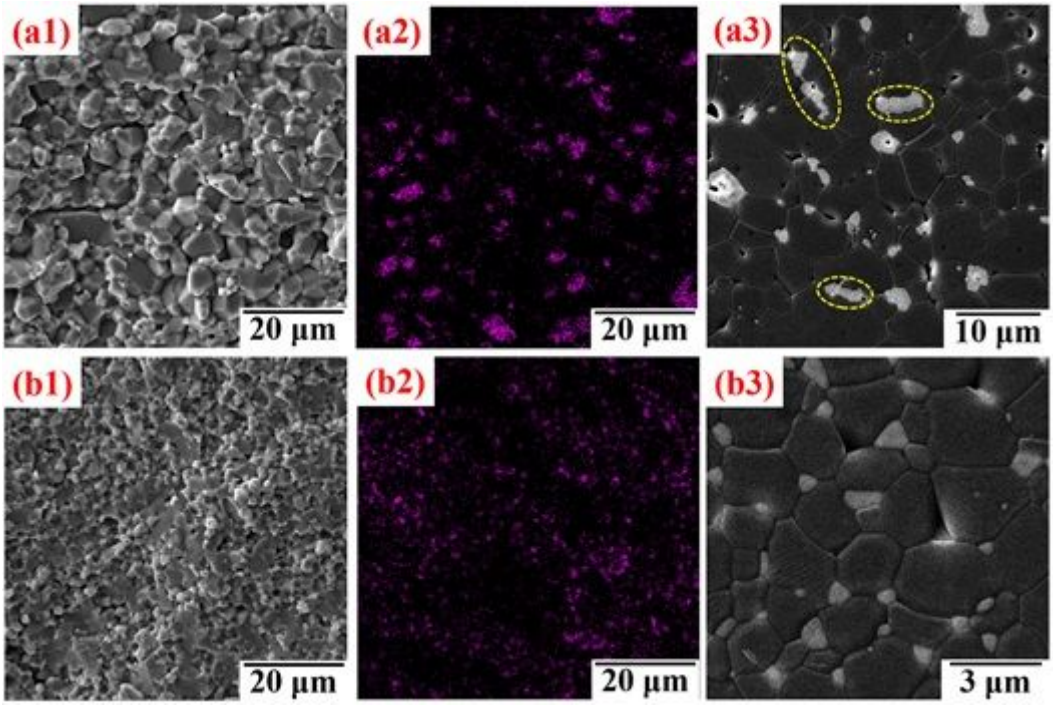

Figure 9

SEM images and corresponding EDS mappings for Y on the fracture surfaces of Sample MM (a1, a2) and Sample CP (b1, b2); SEM micrographs of the polished and etched surfaces of Sample MM (a3) and Sample CP (b3). The semi-connected second phases are marked with red circles.

Figure 10

Optical image of fin-type Al2O3 ceramic heat sinks fabricated by a novel approach integrating DLP-stereolithography and CP process.